SPACE SCIENCES

Water on the surface of the Moon as seen by the Moon Mineralogy Mapper: Distribution, abundance, and origins

Shuai Li* and Ralph E. Milliken

A new thermal correction model and experimentally validated relationships between absorption strength and water content have been used to construct the first global quantitative maps of lunar surface water derived from the Moon Mineralogy Mapper near-infrared reflectance data. We find that OH abundance increases as a function of latitude, approaching values of ~500 to 750 parts per million (ppm). Water content also increases with the degree of space weathering, consistent with the preferential retention of water originating from solar wind implantation during agglutinate formation. Anomalously high water contents indicative of interior magmatic sources are observed in several locations, but there is no global correlation between surface composition and water content. Surface water abundance can vary by ~200 ppm over a lunar day, and the upper meter of regolith may contain a total of ~1.2×10^{14} g of water averaged over the globe. Formation and migration of water toward cold traps may thus be a continuous process on the Moon and other airless bodies.

INTRODUCTION

The presence of H-bearing species, such as OH and H_2O, hereafter referred to simply as "water," in lunar materials and at the lunar surface can record important information about solar wind implantation, impact delivery of volatiles, and the incorporation and retention of volatiles during the accretion and evolution of the Moon (1–4). A variety of observations and measurements over the past decade have presented new evidence for water in the lunar interior (5–15), as well as in the lunar regolith (16–21), demonstrating that endogenous and exogenous sources contribute to the water observed in lunar materials. However, the relative contributions of these sources and how they are manifested at the lunar surface today remain poorly constrained at a global scale.

Lines of evidence for endogenous (magmatic) water have the advantage that they are based on detailed in situ measurements of returned lunar samples, with the drawback that only a small fraction of the Moon has been directly sampled. In contrast, the near-infrared (NIR) reflectance spectra acquired by an orbiting or passing spacecraft can provide a global view of water at the lunar surface through identification of diagnostic OH/H_2O absorptions in the ~2.6- to 4-μm-wavelength region. Although sensitive only to the optical surface (upper ~1 mm), the spatial and temporal coverage allowed by these data can provide information about the occurrence of water associated with ancient magmatic activity as well as dynamic interactions between the lunar regolith and solar wind and/or hydrous impactors.

The NIR reflectance spectra acquired by the Deep Impact/EPOXI (Extrasolar Planet Observation and Deep Impact Extended Investigation) mission, the visible and infrared mapping spectrometer (VIMS) on the Cassini spacecraft, and the Moon Mineralogy Mapper (M^3) instrument on the Chandrayaan-1 mission all exhibit absorptions consistent with fundamental OH/H_2O vibrations in the ~3-μm-wavelength region (18–20), and it has been speculated that these water absorptions are largely the product of interactions between the lunar regolith and solar wind (17–19). It has also been argued that lunar surface OH/H_2O abundance varies on diurnal time scales (18) and that confirming and quantifying this cycling would help establish whether temperature-driven migration of volatiles from low to high latitudes is a viable and ongoing process capable of delivering water to cold traps at the lunar poles (1, 4, 22). If confirmed, water formation via solar wind implantation and its migration across the lunar surface could also have implications for hydrogen implantation and migration on other airless bodies, such as Mercury and near-Earth asteroids, that will be encountered and sampled by the Hayabusa 2 and OSIRIS-REx (Origins, Spectral Interpretation, Resource Identification, Security, Regolith Explorer) missions.

The extent to which the Moon can be used as a baseline to understand water-related phenomena on other airless bodies is dependent on our ability to accurately identify, map, and quantify the spatial and temporal distribution of OH/H_2O at the lunar surface. The M^3 data set provides the most complete spatial and temporal NIR coverage of the Moon that currently exists and is likely to exist in the near future; thus, it is the best data set to address questions related to surface OH/H_2O and is the focus of this study. However, lunar NIR spectra are commonly affected by the presence of thermally emitted radiation at wavelengths of >2 μm, and difficulties associated with quantifying and removing this thermal contribution have complicated previous attempts to identify and quantify water absorptions at a global scale (17, 23, 24). Unless properly removed, thermal emission can weaken, distort the shape of, or even mask absorptions in the ~2- to 5-μm-wavelength region (17, 23, 24), precluding accurate mapping of lunar surface water.

Previous studies of M^3 (17, 19) and other NIR data (18, 20) have used first-order thermal corrections that have provided a revolutionary view of water on the Moon, but uncertainties in these methods have resulted in ambiguity and conflicting points of view about the distribution and mobility of this water. The strongest OH/H_2O absorptions were observed to occur at higher, colder latitudes (19, 20), but it has also been noted that such a latitude dependence may be the result of incomplete thermal removal due to the anisothermality of the lunar regolith (25). Similarly, Deep Impact flyby data exhibit different absorption strengths for different local times of day, which has been interpreted to represent the accumulation and subsequent loss/migration of lunar water as a function of instantaneous rather than average temperature (18). However, effects due to viewing geometry and thermal emission could be responsible for some of the observed spectral differences (20),

Department of Earth, Environmental, and Planetary Sciences, Brown University, Providence, RI 02912, USA.
*Corresponding author. Email: njushuaili@gmail.com

which could negate evidence for diurnal mobility of surface OH/H_2O in these data. Conflicting reports also exist as to whether brighter anorthositic highland terrains exhibit stronger water absorptions compared with darker basaltic mare terrains (17–19), a correlation that could be due to nonlinear absorption and scattering effects at NIR wavelengths as opposed to inherent differences in water content or composition-dependent interactions between the lunar regolith and solar wind (26).

Recent comparisons with independent surface temperature estimates from overlapping Lunar Reconnaissance Orbiter (LRO) Diviner radiometer data indicate that previous thermal correction models for M³ data (27) commonly underestimate surface temperatures by ~10 to 30 K (23, 25) and thus cannot be used for accurate assessments of OH/H_2O at a global scale. These results also confirm previous concerns that the current publicly available M³ spectra contain residual thermal effects (17), and we have addressed these issues by applying a new thermal correction model to the M³ data (23). The newly reduced data are used to produce the first global quantitative maps of lunar surface water, yielding new information on its distribution, mobility, and likely origins.

Theory and experimental data suggest that the retention of OH/H_2O on the lunar surface may depend on a variety of factors, including surface temperature (2), composition (2), crystallinity (28), and degree of space weathering (29). We evaluate these and other relationships at a global scale by mapping the strength of OH/H_2O features in the thermally corrected M³ spectra after those data have been converted to single-scattering albedo (SSA) via the Hapke radiative transfer model (see Methods for details) (30). The SSA spectra are advantageous compared with the reflectance spectra because they explicitly account for the variations in viewing geometry, reduce the effects of multiple scattering, and reduce the correlations between albedo and absorption strength that are not related to the abundance of the absorbing species. The effective single-particle absorption-thickness (ESPAT) parameter is a measurement of absorption strength based on the SSA spectra (30), and laboratory measurements of hydrated phases and lunar-relevant materials confirm that its value at ~2.9 μm is linearly related to OH/H_2O content (see Methods). The ESPAT parameter is thus a linear proxy for water content in which the slope of the ESPAT–weight % H_2O relationship varies as a function of particle size (fig. S1). We present results for the M³ data in terms of both ESPAT values and weight % H_2O, where the latter is based on assuming that the irregularly-shaped particles have a diameter of 60 to 80 μm for the lunar regolith, a range that is consistent with average grain sizes measured for Apollo soils (31).

RESULTS

Global spatial distribution of lunar surface water

A quantitative global map of water at the optical surface of the Moon, as determined from the M³ spectra, the first of its kind, is presented in Fig. 1 and demonstrates that OH/H_2O absorption strength at ~2.9 μm increases as a function of latitude. This latitude dependence is broadly consistent with previous studies of the M³ data (17, 19), but the improved thermal correction model allows for a more accurate estimate of absorption strength and water content at low latitudes, where surface temperatures can exceed 400 K. We observe that water absorptions are commonly very weak or absent in the spectra for the ±30° latitude zone (Fig. 1B) but increase sharply at higher latitudes, corresponding to maximum water abundances of ~750

and ~500 parts per million (ppm) for the Northern Hemisphere and Southern Hemisphere, respectively (Fig. 1B).

The apparent asymmetry in water content between the Northern Hemisphere and the Southern Hemisphere, as seen in the M³ data, is in accordance with the variations in the suppression of epithermal neutrons, as seen in the Lunar Prospector data [stronger suppression in the Northern Hemisphere, consistent with increased H abundance (32)]. In contrast to mid- and high latitudes, estimates of water abundance for regolith at latitudes of <30° are commonly <100 ppm, consistent with the values measured for returned lunar samples (Fig. 2). We observe no indication that OH/H_2O absorption strength varies systematically as a function of longitude (Fig. 1C), although the specific latitude at which water abundance begins to increase does vary with longitude.
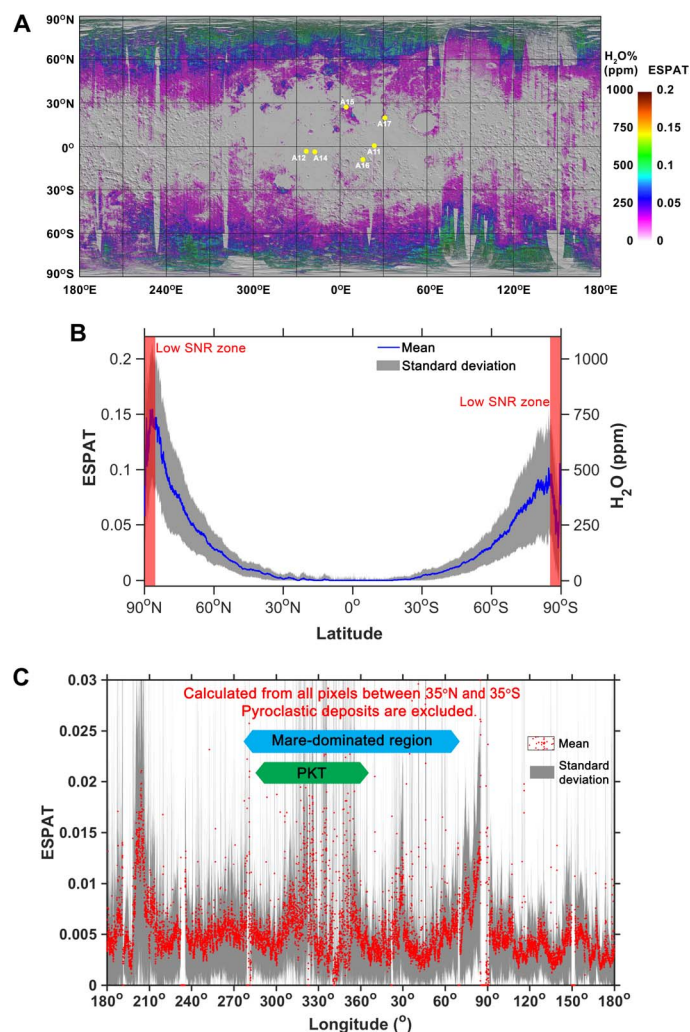
Fig. 1. Water content of the lunar surface as derived from the M³ data. (A) Global map of ESPAT values (at ~2.86 μm) and estimated water contents (assuming that the irregularly-shaped particles have a diameter of 60 to 80 μm) calculated from the M³ data overlain on a Lunar Orbiter Laser Altimeter shaded-relief map. Apollo landing sites are labeled with yellow dots. (B) Latitude profile of ESPAT and water content derived from (A) when averaged over all longitudes. (C) Longitude profile of ESPAT values averaged over all latitudes between 35°N and 35°S. Light blue bar indicates the approximate latitude range of mare dominant region. The green bar shows the approximate latitude range of PKT. PKT, Procellarum KREEP Terrane.

Comparison of water content with regolith maturity

Optical maturity (OMAT) is a spectral parameter that has been devised to estimate the degree of space weathering for lunar soils based on reflectance properties at visible-NIR wavelengths (33). Figure 3 presents plots of OMAT values previously derived from the Clementine multispectral data (33) versus our ESPAT values calculated from the M^3 data. Higher OMAT values are interpreted to represent "immature" soils, whereas accumulation of submicroscopic nanophase Fe during enhanced space weathering leads to more "mature" soils and lower OMAT values. Although OMAT values cannot indicate exposure ages older than Copernican (~1.2 billion years ago) (33), they are roughly indicative of maturity for typical lunar particles with mean sizes of 60 to 80 μm (34) and provide a useful proxy for relating water absorption strength to likely degree of space weathering.

No correlation between OMAT and ESPAT (water content) is observed for latitudes lower than ±30°, consistent with the general lack of strong OH/H_2O absorptions in this latitude range. In contrast, regions of increased maturity (lower OMAT) exhibit increased water contents (higher ESPAT) for latitudes in the range of ~60° to 70° for both hemispheres (Fig. 3). A similar but weaker correlation between maturity and water content is also observed for mid-latitudes. These trends suggest that when surface OH/H_2O is present in sufficient amounts, as is the case for latitudes poleward of ~30°, its abundance increases as a function of the maturity of the lunar regolith. At a latitude of 60° to 70°, the ESPAT values (and associated water contents) vary by a factor of ~3 (~0.02 to 0.06) over the observed OMAT range, and it is also evident that bright rays associated with young craters exhibit weaker water absorptions compared with surrounding terrains (Fig. 3, C and D). This is true, even at mid- and high latitudes where absorptions are strongest, whereas soils at low latitudes are relatively dry regardless of OMAT. These results indicate that latitude is the primary control on surface OH/H_2O abundance but that soil maturity is an important secondary factor.

Comparison of water content with surface composition

Contrary to previous studies of the M^3 data, we observe no strong differences in water content between mare and highland regions at a global scale (Fig. 1). As noted above, most variations in OH/H_2O
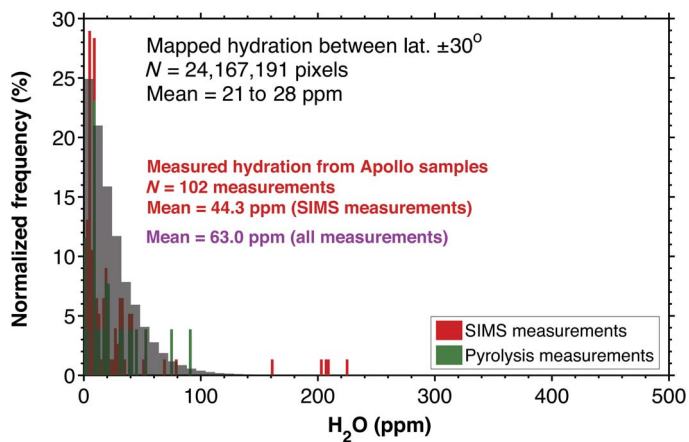
Fig. 2. Comparison of M^3-derived water contents for the ±30° latitude zone, which includes Apollo sampling locations, with water contents measured from bulk Apollo samples (see tables S1 and S2 for individual values and references).

at the optical surface can be described as a function of latitude or OMAT. If water is present in the bulk mantle, then KREEP (potassium, rare earth element, and phosphorous)–like components linked to the last stages of magma ocean cooling are expected to be enriched in water (35), as would magmas of evolved composition. We observe no strong increase in water associated with the PKT as a whole (Fig. 1C), but we do observe that several features previously interpreted as silicic domes exhibit increased OH/H_2O absorptions compared with surrounding terrains (Fig. 4). In addition, some (but not all) regions, where crystalline plagioclase exposures have been identified (36), correspond to zones of enhanced hydration (Fig. 5 and fig. S2).

Despite the general lack of correlation between composition and water content, there is a notable exception that is observed even at the global scale. Nearly all large lunar dark mantle deposits, inferred to represent pyroclastic deposits enriched in volcanic glass (37), exhibit water contents that are anomalously high compared to surrounding terrains regardless of latitude and OMAT (Fig. 1) [(38), chap. 3; (39)]. Similar to water detected in the central peak of the Bullialdus crater (40) and an inferred silicic volcanic complex at Compton-Belkovich (41, 42), water in these deposits likely originated from magmatic sources and not from solar wind implantation.

Diurnal variations in water content

The fraction of the Moon that was imaged by M^3 at different local times of day is small, making it difficult to assess the possibility of diurnal variations in OH/H_2O at a global scale. However, the region from 90°N to 90°S and ~200°E to 300°E was viewed at three different local time periods: morning (6:00 to 10:00 a.m.), noon (10:00 a.m. to 2:00 p.m.), and afternoon (2:00 to 6:00 p.m.) (fig. S3). ESPAT values and water content as a function of latitude for each time of day are presented in Fig. 6. Only pixels for latitudes between ±70° were plotted due to an insufficient number of the M^3 spectra of appropriate quality near poles. Both the morning and afternoon data exhibit increased absorption strengths compared with the spectra acquired near local noon, particularly for latitudes equatorward of 60°N/60°S. At a higher latitude, there is no clear diurnal variation of lunar surface water, at least for the region and times associated with these M^3 data.

The higher water content for the morning data compared with the afternoon data may be due to the latter being acquired closer to local noon relative to the former (Fig. 6B), leaving less time for reaccumulation of water. The difference in acquisition time between the morning and afternoon data relative to local noon is also slightly smaller for the Southern Hemisphere (0.1 hour) than the time difference for data in the Northern Hemisphere, which may also explain the smaller difference in water content between the morning and afternoon data that is observed for southern latitudes relative to northern latitudes (Fig. 6A).

Spectra for latitudes between ±60° exhibit the strongest diurnal variation in hydration, and the range is largest for mid-latitudes and smallest for equatorial latitudes. When compared with the global map in Fig. 1, this suggests that equatorial latitudes may contain some amount of surficial water during early morning and late afternoon, consistent with the Deep Impact observations (18), but that the ±30° latitude zone is generally OH/H_2O-poor and especially so near local noon. In contrast, latitudes of >±60° exhibit the highest water contents, and this water may be largely stable over the course of a lunar day. Locations within the 30°- to 60°-latitude range exhibit the largest dynamic range in absorption strength (Fig. 5, C and D) for both hemispheres, equivalent to a loss/gain of up to ~200 ppm
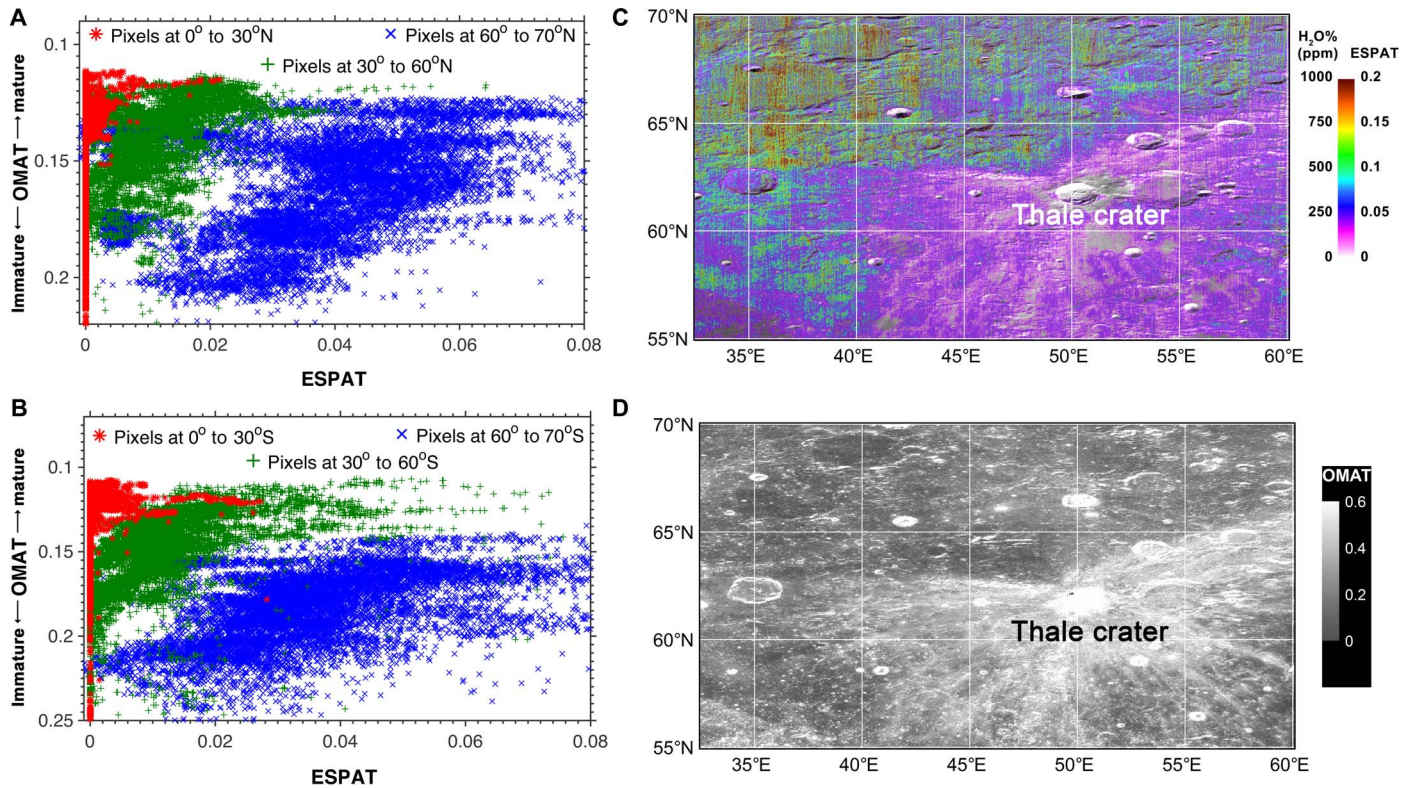
Fig. 3. Comparison of water content (ESPAT) with OMAT of lunar regolith. Scatterplot of M³ data for (**A**) the Northern Hemisphere and (**B**) the Southern Hemisphere. Example map of (**C**) water content and (**D**) OMAT for the Thale crater showing spatial coherence between immature regolith and low water content.
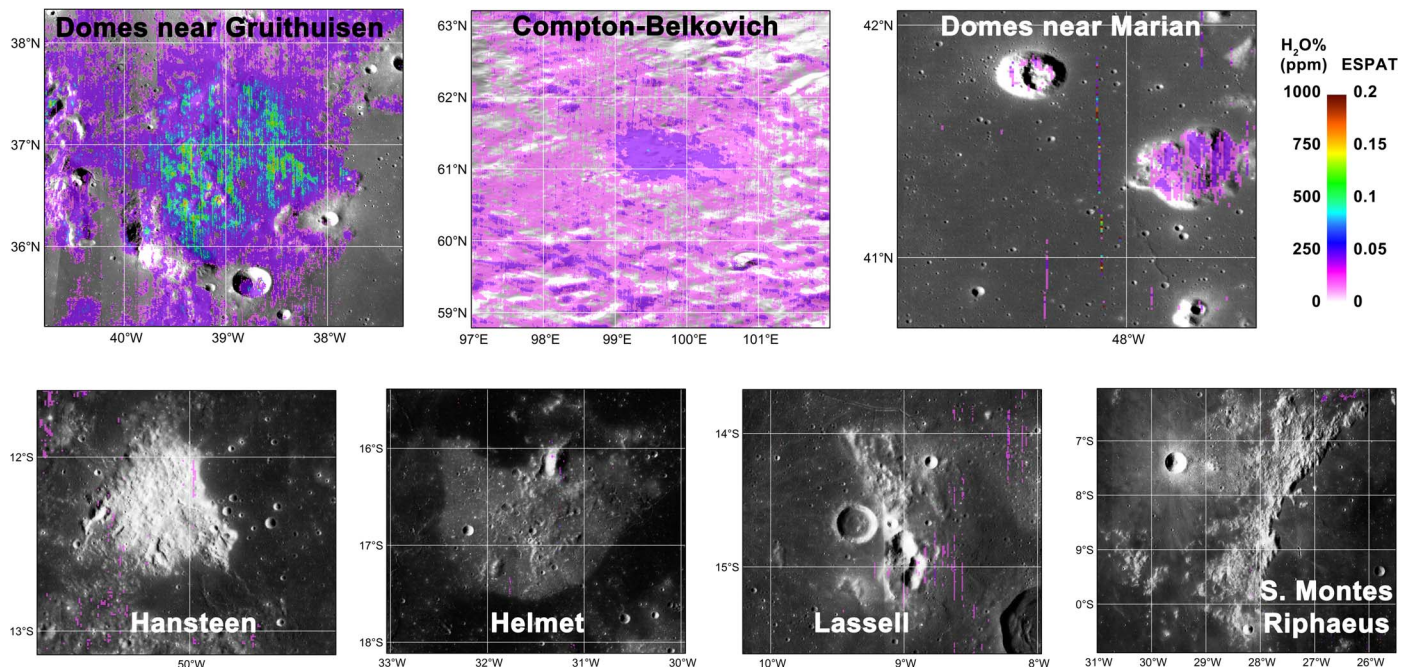
Fig. 4. Water content maps for previously reported silicic domes (49, 50). Features at Gruithuisen, Compton-Belkovich, and Maria exhibit anomalous increases in water content that is suggestive of volatile-rich magma sources, whereas other purported silicic domes lack evidence for increased hydration.

of water between local morning, noon, and afternoon, assuming that the particles have a diameter of 60 to 80 μm.

DISCUSSION

The distribution and variation in lunar surface water are primarily correlated to latitude (Fig. 1), which is a spatial manifestation of control by temperature. The latitudinal variation of lunar surface water may be associated with a decrease in diffusion and thermal desorption at lower temperatures toward the poles. This apparent temperature dependence is consistent with NIR observations by Deep Impact (18), as well as the presence of increased hydrogen observed in the upper tens of centimeters of the regolith near the poles in the neutron data (32). However, variations in ESPAT/water content for latitudes of >±85° cannot be reliably determined from the M^3 data due to significant shadowing and low signal-to-noise ratios (SNRs). Regardless, it is clear that the diurnal variations in water absorption strength become weaker and that water stability increases toward the poles in both hemispheres, consistent with increased water retention and accumulation due to lower temperatures, slower diffusion, decreased sputtering, or some combination of these factors.

Far-ultraviolet (UV) data acquired by the Lyman Alpha Mapping Project (LAMP) also exhibit diurnal variations in surface hydration that weaken at latitudes of >60° (43–45), although the LAMP-sensing depth is several orders of magnitude smaller (<100 nm) than M^3. LAMP data have been interpreted to represent mobility of H$_2$O, primarily because Lyman-α and far-UV properties of H$_2$O ice are known, whereas properties of OH and H$_2$O adsorbed on or structurally bound within minerals are not (43, 46). However, the LAMP data do not preclude OH as being responsible for the observed signal, and confirmation by two independent NIR instruments (Deep Impact and M^3) strongly supports the formation and destruction of H-bearing species across the lunar surface on diurnal time scales. We note that OH itself is not required to be mobile to explain the decrease in M^3 absorption strength; the loss of H$^+$ alone by breaking of O–H bonds (leaving behind highly reactive oxygen sites) would yield a similar spectral signature at NIR wavelengths.

The spatial distribution and temporal variation of OH on the Moon, as seen in the M^3 data, are consistent with solar wind being the dominant source of lunar surface water, although enrichments associated with pyroclastic deposits [(38), chap. 3; (39)], silicic regions (41, 42), and crater central peaks (40) indicate that local surface expressions of magmatic water are present as well. Agglutinates contain water (16), and their abundance increases with soil maturity (degree of space weathering) (34); therefore, it may be expected that the bulk water content of lunar regolith also increases as a function of maturity. This is the trend observed in the newly corrected M^3 data at mid-to-high latitudes—areas where surface water stability increases exhibit a positive correlation with soil maturity, as inferred from the OMAT parameter (Fig. 3). Experimental results suggest that the efficiency of hydroxyl formation from solar wind implantation may also increase with soil maturity (29), representing another factor that may contribute to this correlation.

We propose that agglutinates are an important and perhaps the primary host of water responsible for absorptions seen at latitudes of >30° (Fig. 1). The lack of similar water signatures for soils of similar maturity at low latitudes suggests that agglutinates in these regions lose water over time, are less efficient at trapping water during their formation, and/or form from materials poorer in OH/H$_2$O compared with higher-latitude counterparts. The latter is consistent with the observed decrease in diurnal variation of surface water at higher latitudes. This indicates that more water of solar wind origin may be present in soils at those locations due to its increased stability at the lunar surface, and isotopic measurements of water in agglutinates confirm that they contain a solar wind component (16). Therefore, the more solar wind–derived water that is present in a soil during a micrometeorite impact event, the more water there exists to be trapped/quenched in the resulting agglutinitic glass.

This model predicts that agglutinates formed at higher latitudes contain more OH/H$_2$O than those formed at lower latitudes, a hypothesis that can be tested by future sample return. This model also implies that water abundances in bulk agglutinates within the Apollo samples, which are all from latitudes of <30°, are near the detection limit of M^3 (~20 ppm based on the assumptions made here; see Methods). Excluding areas enriched in water that may be associated with magmatic sources, our estimated water contents in the ±30° latitude zone are commonly <100 ppm, which is similar to the values measured in Apollo soils via pyrolysis and similar to the ~70 ppm of water estimated for regolith based on secondary-ion mass spectrometry (SIMS) measurements of lunar agglutinates (Fig. 2) (16). In contrast to mid- and high latitudes where bulk agglutinates may have higher water contents, the M^3 signature observed at low latitudes, and the diurnal variations, in particular, may be dominated by water in the outermost 100 to 200 nm of regolith grains (including agglutinates) that is most sensitive to solar wind implantation and sputtering. This effect would also explain why similar diurnal variations are observed for the upper ~100 nm in the LAMP data at low latitudes.

In summary, the M^3 signatures are likely dominated by two components. First is the bulk water content of agglutinitic glass, which may be stable over diurnal cycles and contains a solar wind component trapped/quenched during formation, and second is the water in grain rims that is dynamic over diurnal cycles due to ongoing regolith–solar wind interactions. The relative contribution of these two components to the NIR data varies as a function of latitude due to variations in surface temperature and solar wind flux, and the bulk
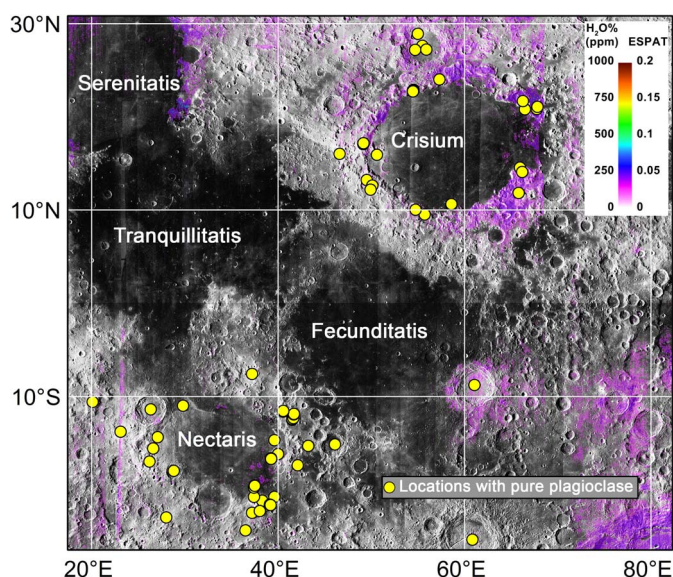
Fig. 5. Comparison of M^3-derived water map with previously reported exposures of crystalline (unshocked) plagioclase (36) near Mare Crisium and Mare Nectaris.

agglutinate component dominates the spectral signature at high latitudes, whereas the grain rim component dominates at equatorial latitudes. Soils at mid-latitudes (±30° to 60°) have significant contributions from both components, as evidenced by their increased water abundance and large dynamic range in water content over diurnal cycles.

Previous studies of the M^3 data have suggested that plagioclase-rich locations may exhibit increased water contents (19), but a comparison of the new water content maps with previously reported occurrences of unshocked plagioclase shows no clear correlation (fig. S2). There are several exceptions, including highland terrains surrounding Mare Crisium, where a zone of increased water content includes a number of plagioclase-rich outcrops (Fig. 5). However, there is not a one-to-one correlation between individual outcrops and water content, and increased water contents are not observed for similar outcrops in the nearby Mare Nectaris. Water measured in the plagioclase grains of lunar anorthosite has been interpreted as evidence for as much as 320 ppm of water in the lunar magma ocean (15). The weak links between the M^3-derived water abundance and some plagioclase-rich outcrops are tantalizing observations that may support this interpretation of a wet early Moon, but as a whole, the M^3 data do not provide clear evidence for magmatic water in the anorthositic crust.

In our corrected data, we observe no significant differences in water content between mare and highland regions (Fig. 1), although these trends cannot be ruled out if they are within the uncertainties of the methods presented here or if any expected differences are smaller than the detection capabilities of M^3. Compositional trends observed in previous M^3 studies of surface water may be an artifact of nonlinear absorption and scattering that influences absorption strength in the reflectance spectra, whereas these effects are greatly reduced by using ESPAT derived from the SSA spectra (26, 47). If not properly accounted for, absorption strength determined from the reflectance spectra can give the false impression that bright regions have stronger absorptions compared with dark regions, an effect that has also been observed for Mars (26).

At smaller spatial scales, hydration absorptions in the M^3 spectra for 3 of 11 lunar swirl features were previously shown to exhibit a stronger OH absorption near 2.8 μm compared with the spectra from surrounding terrains, suggesting that localized magnetic anomalies may weaken solar wind interaction with regolith at lunar swirls (48). We do not observe this trend for lunar swirls between the ±30° latitude, where water absorptions are typically weak or absent, but we do confirm it for a mid-latitude lunar swirl at Mare Ingenii (Fig. 7). Although the spectral differences are small, M^3 pixels with the weakest absorptions exhibit a spatial coherence that matches the location of swirls. This is consistent with weakened solar wind interaction at lunar swirls, but the effect on water content is only apparent at mid- and high latitudes, where water can accumulate in adjacent terrains
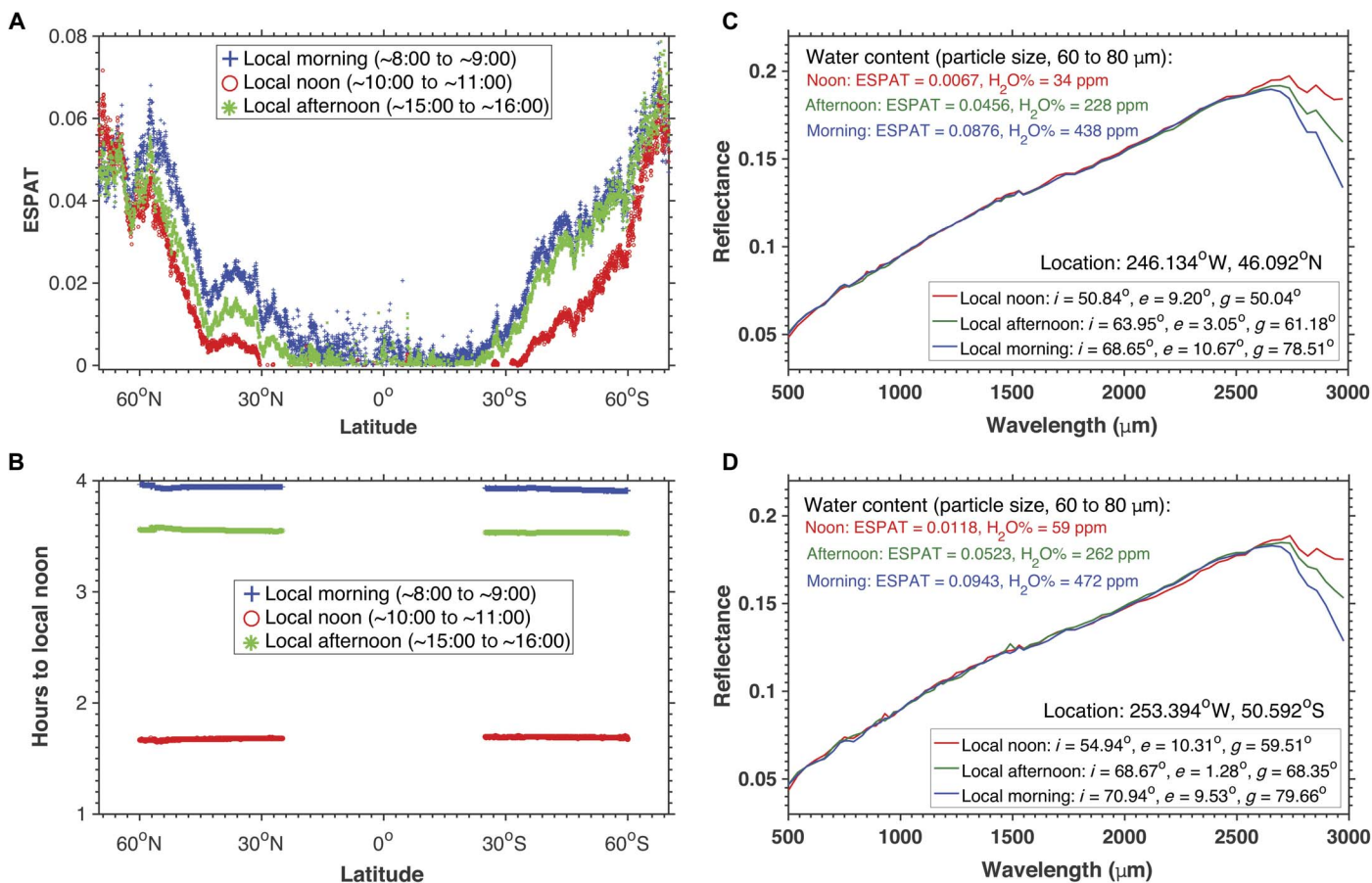
Fig. 6. Diurnal variations in water content of the lunar surface. (**A**) Averaged ESPAT/water content values from 70°N to 70°S latitude at different local times of day (maps are shown in fig. S3). (**B**) Absolute number of hours relative to local noon for the M^3 data used in (A). The example spectra acquired at the same location at different local times of day from (**C**) the Northern Hemisphere and (**D**) the Southern Hemisphere show diurnal variations in the strength of OH/H_2O absorptions near ~3 μm. i, solar incidence angle; e, emittance angle; g, phase angle.

due to increased stability. Similar trends may exist at another high-latitude swirl at the Hopmann crater (49°S, 160°E), but we cannot confirm this due to incomplete M^3 coverage at this location.

Anomalously strong water absorptions are observed for a number of lunar pyroclastic deposits [(38), chap. 3; (39)], demonstrating that water sourced from the lunar interior can be identified and quantified using the new thermally corrected M^3 data. Hydration anomalies were also previously observed at a high-latitude volcanic complex at Compton-Belkovich (41, 42) and at the central peak of the Bullialdus crater (40), both of which were attributed to magmatic sources. We confirm both of these detections and estimate the water content at Bullialdus to be <250 ppm (Fig. 8) based on the methods presented here. Our estimated water content for silicic volcanic deposits at Compton-Belkovich is ~200 to 250 ppm, approximately ~100 ppm higher than the surrounding terrains at this high latitude (Fig. 4).

We also observe increased water contents at two of six other previously reported silicic volcanic constructs (49, 50), the Marian and Gruithuisen domes, neither of which has previously been reported to contain water. Several factors may explain the lack of water observed for the other four regions, including volatile loss during magma degassing, water-poor magma source regions, or misidentification of these constructs

as evolved magma compositions. Regardless, these new observations confirm that some silicic and KREEP-related lithologies on the Moon contain enhanced water contents, consistent with enrichment in volatiles during magmatic evolution. However, the PKT as a whole does not exhibit enhanced water content (Fig. 1C); thus, whether these observations reflect bulk properties of the lunar magma ocean or localized magma sources with anomalously high water contents remains unclear.

Hydration anomalies associated with impacts are not typically observed at the scale of the M^3 data, indicating that either large hydrous impactors have had no significant contribution to the surface-volatile reservoir in the recent geologic past or these volatiles have since been removed and/or redistributed across the lunar surface. Two notable exceptions are the craters Copernicus and Plato, both of which exhibit increased water content that may reflect retention of volatiles from hydrous impactors and are deserving of future study.

Because of their different stabilities, differentiating among OH, molecular H_2O, and H_2O ice at the lunar surface is critical for understanding the formation, accumulation, and migration of lunar water, as well as its extraction potential for in situ resource utilization. NIR absorptions considered diagnostic for hydroxyl and molecular H_2O were previously studied in the VIMS and M^3 data in an attempt to differentiate
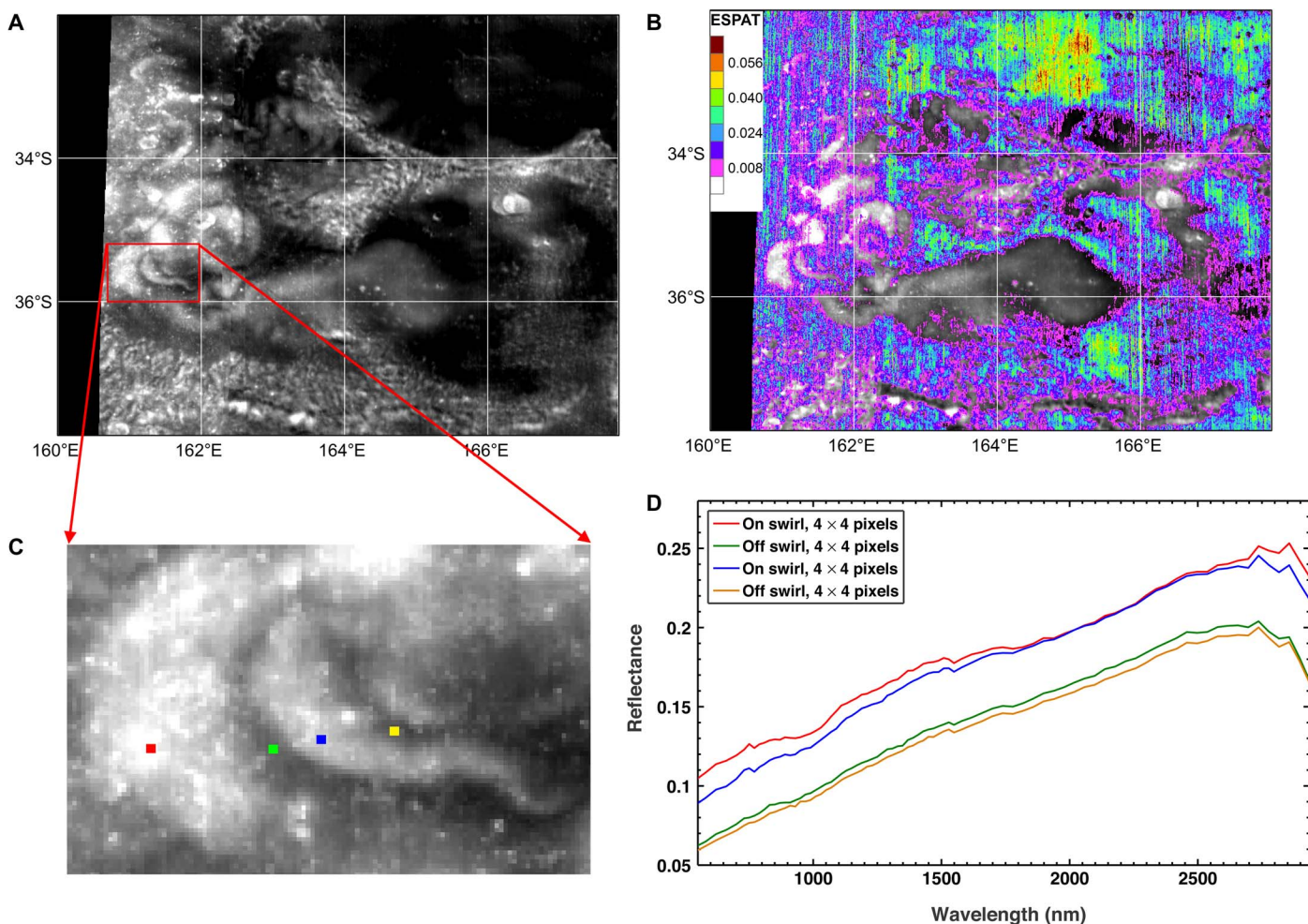
Fig. 7. Estimated water content for lunar swirl at Ingenii. (**A**) Albedo map (750 nm) from the LRO Wide Angle Camera (WAC) mosaic. (**B**) M^3 water map overlain on albedo map. (**C**) Zoomed-in view of swirl showing locations for (**D**) examples of the thermally corrected M^3 spectra.

and map these species (*17*), and it has also been argued that variations in these species may be correlated with composition and latitude.

Absorptions due to OH vibrations commonly occur at wavelengths of ~2.65 to 2.9 μm, whereas fundamental stretching vibrations of H_2O occur near ~2.9 μm, and the first overtone of the H_2O bending vibration occurs near ~3.1 μm. However, the position and strength of OH absorptions are highly variable, and they can occur at wavelengths of >2.9 μm, depending on the bonding energy and the cation to which the hydroxyl is attached; thus, OH absorptions may be broad and occur throughout the ~2.65- to 3.5-μm range (*51*). Excluding the final wavelength channel of M^3 (band 85, 2.976 μm), which is near the edge of the detector and has a lower SNR (*52*), the longest wavelength measured in these data is 2.936 μm. Hence, the wavelength range of M^3 is too limited to accurately determine the full shape and maximum absorption point within the 3-μm region, making it difficult to differentiate OH from H_2O, particularly if both species are present.

After the implementation of the new thermal correction model, we find that water absorptions in the resulting M^3 spectra are largely similar in shape across the lunar surface and vary primarily in strength. Occurrences of discrete OH bands identified in previous studies, differentiated from H_2O by their increase in reflectance in the last several wavelength channels of the M^3 data, may have been an artifact of incomplete thermal removal. Therefore, the existing M^3 data are best interpreted as representing the presence and distribution of OH and provide no unambiguous evidence for the presence of H_2O.

Because of the radiolysis of H_2O and the higher thermal stability of OH, the latter may be expected to be the dominant species at the optical surface based on theoretical considerations and laboratory experiments (*28*, *53*). However, the VIMS and Deep Impact NIR data for the Moon, although of lower spatial resolution than M^3 and only acquired during flyby opportunities, both exhibit broad absorptions in the 3-μm region that may be due, in part, to the presence of molecular H_2O. Whether H_2O is present at the optical surface thus remains an outstanding question, and further study of the VIMS and Deep Impact data is warranted.

The M^3 data and maps presented here provide a critical quantitative foundation for assessing lunar water at a global scale, a necessary first step in evaluating whether this water can be used as an in situ resource for human exploration. If our globally averaged latitude profile for water (Fig. 1B) is assumed to extend to 1-m depth due to regolith gardening and the regolith density is on the order of 1.8 g/cm³, then as much as 1.2×10^{14} g of water may be present in the upper meter of regolith when averaged over the entire Moon. This is near the upper end of estimates of surface water modeled by Hodges (4×10^{12} to 2×10^{14} g) (*22*) and is an order of magnitude lower than the mass estimated to be in the polar regions from the neutron data (*32*). The total amount of water in the lunar regolith is thus a significant reservoir and may be large and dynamic enough over geologic time scales to act as the source of water currently observed at the poles, but it is not as highly concentrated as the water in those regions. Although implanted and mobilized on diurnal cycles, the correlation with soil maturity also indicates that much of the surface water present today is not renewable on short time scales. These characteristics may present challenges for use as an in situ resource, but large pyroclastic deposits with high water contents may provide viable nonpolar alternatives.
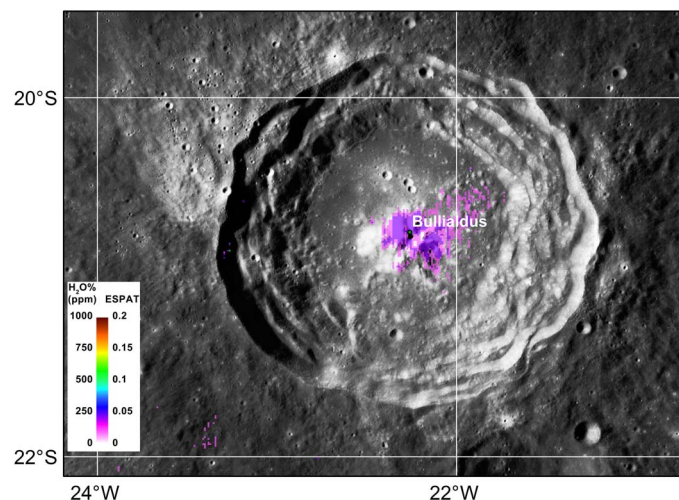
Our results also demonstrate that localized occurrences of magmatic water can be identified from an orbit and occur in a variety of locations on the Moon, providing new evidence for water in the lunar mantle, but at the spatial scale of the M^3 data, we find no strong correlation between water content and KREEP terrains that would indicate widespread concentration of water during late-stage crystallization of the lunar magma ocean. Rather, water in the lunar regolith contains a dynamic component and is most consistent with OH originating from solar wind implantation of H^+, and similar processes may occur on other airless planetary bodies. However, the presence and mobility of molecular H_2O on the lunar surface remain unclear based on the existing NIR data, and future orbital instruments that span the ~3- to 4-μm-wavelength range and provide global, time-resolved coverage are required to fully differentiate and determine the dynamics of OH, molecular H_2O, and H_2O ice on the Moon.

In summary, we find that OH abundance increases primarily as a function of latitude and secondarily as a function of soil maturity (degree of space weathering). This is consistent with solar wind being the dominant source of lunar surface water, and agglutinates in the lunar regolith are likely the primary host of this water. Mare and highland regions exhibit similar absorption strengths at a global scale, indicating that implantation and retention of water originating from solar wind processes are largely independent of composition at the spatial scales of the M^3 data. The formation and removal of surface OH are confirmed to be dynamic over the course of a lunar day, likely as a result of solar wind sputtering and/or other temperature-dependent processes. Finally, KREEP terrains generally do not exhibit increased water contents, but pyroclastic deposits and some previously reported silicic domes exhibit anomalously strong water absorptions that are indicative of internal (magmatic) sources. These results provide a new quantitative foundation for comparison with theoretical calculations, experimental studies, and independent observations of volatiles on the Moon and other airless bodies.

Fig. 8. Water content map for Bullialdus crater exhibiting increased hydration in central peak, approaching values of ~250 ppm.

METHODS
Overview of the thermal correction model for the M^3 data
A new semi-empirical thermal correction model for the M^3 data was developed on the basis of the laboratory reflectance spectra of the Apollo and Luna samples, and this model was independently validated with a radiative transfer model in conjunction with lunar surface

temperatures measured by the Diviner instrument on the LRO (23). According to the correlation between the reflectance values at 1.55 µm (band 49 of M^3 images) and those at 2.54 µm (band 74 of M^3 images) of the laboratory spectra and the M^3 data corrected using Diviner temperatures, the reflectance values observed at 1.55 µm in the M^3 data can be used to predict the reflectance values at 2.54 µm, and any excess reflectance at the longer wavelengths can then be estimated and removed from the original radiance data before conversion to surface reflectance (23). A key benefit of this model is that the M^3 data can be thermally corrected without the need for independently measured surface temperatures acquired at the same local lunar time of day. Full details and examples of this process, as well as a discussion of potential thermal effects in the M^3 data due to surface roughness, resulting in anisothermality, are provided in the study of Li and Milliken (23).

Deriving water abundance from the reflectance spectra
Identification and quantification of water from the reflectance spectra are commonly based on fundamental OH and H_2O stretching absorptions observed near ~2.9 µm. However, the strength of water absorptions in the reflectance spectra may be affected by multiple scattering, albedo variation, viewing geometry, particle size, and possibly composition (26, 47, 54, 55). Previous studies have demonstrated that ESPAT (54), calculated at a wavelength of ~2.9 µm from the spectra (54), exhibits a linear correlation with water content for a wide variety of hydrous materials, where the slope of the trend line varies as a function of particle size (26, 47, 55). By building on this previous work, we recently carried out new laboratory experiments and simulations to determine specific ESPAT–weight % H_2O trends for compositions directly relevant to the Moon, including water-bearing volcanic glasses (terrestrial and synthetic lunar compositions) and anorthosite (see the Supplementary Materials and Methods), and for particle sizes that typify lunar soils (fig. S1). We direct the reader to the full details of this methodology, as provided in chapter 2 in the study of Li (38, 39), which builds on previous studies (26, 47, 55, 56).

Mapping of lunar surface water with the M^3 data
Mapping of lunar surface water with the M^3 data was carried out in two steps. ESPAT parameter values were first derived from M^3 data band 82 (~2.85 µm) after converting the reflectance spectra to SSA, identical to methods described in (38). Lunar surface water was then mapped by applying the determined ESPAT–weight % H_2O slope for 60- to 80-µm-diameter particles (see fig. S1) to the derived ESPAT parameter map. The resulting map was further improved by filtering the data to minimize the effects of several complicating factors, including known spectral artifacts and low SNR for some M^3 data (for example, the spectra acquired under poor solar illumination). The 1.55- and 2.54-µm wavelengths (bands 47 and 74 of the M^3 data, respectively) were used to remove thermal effects based on the methods of Li and Milliken (23), but some pixels exhibited an anomalous decrease in reflectance at band 47 and/or band 74, as shown in the schematic plot in fig. S4. Because the exact reflectance value of band 47 or 74 for these pixels was unknown, we masked all pixels if they have this type of artifact. Pixels exhibiting this type of artifact were concentrated at the polar regions (fig. S4B), suggesting that the effect may be due to the low SNR of the M^3 data at these areas where solar illumination is weak.

To remove the pixels associated with low signal, which may lead to false-positive detections of absorptions, we calculated an SNR index (SNRI) based on the difference between the measured spectra and versions that have been smoothed with a cubic spline algorithm (57)

$$\text{SNRI} = \left(\sum_{i=2}^{73} \text{abs}\left((r_i' - r_i)/r_i' \right) \right) \Big/ 72 \qquad (1)$$

where r_i' and r_i are the reflectance values from the smoothed and measured spectra at band i, respectively. Wavelengths of >2.5 µm were not included in the index calculation because of the potential propagation of artifacts at band 47 to water absorption bands centered at ~2.9 µm during the thermal removal of the M^3 data. Example spectra showing different SNRI values are presented in fig. S5. An empirical limit of SNRI of >0.1 was chosen to mask pixels with low signal. Pixels that were above this threshold and thus masked from the final M^3 maps are shown in fig. S5B; nearly all are concentrated near the poles, as expected, given the low illumination conditions and thus lower signal in these regions.

ESPAT values for each pixel in the regions of interest studied by Li and Milliken (23) were calculated on the basis of the M^3 spectra that were thermally corrected using the Diviner surface temperatures. These values were then compared with the ESPAT values derived from the M^3 data that were thermally corrected using the empirical approach described by Li and Milliken (23), which may lead to a ±2% uncertainty in reflectance. Results of this comparison show that ESPAT values calculated from thermally corrected spectra based on the empirical method may differ by 20% (relative) compared with the ESPAT values determined from the spectra corrected using actual Diviner-based temperatures. Because conversion of ESPAT to weight % H_2O is a simple scalar (the value of which is particle size–dependent), the relative uncertainty in estimated water content that is associated with potential uncertainty in the ESPAT values propagated from uncertainty in the thermal correction is also 20%.

Detection limits of the M^3 data in terms of absolute water content are difficult to quantify because they are dependent on model assumptions and relationships between water content and ESPAT values (for example, particle size). However, the ESPAT values were derived directly from the spectra, and the detection limit for a water absorption (that is, at what absorption strength is a feature outside of the noise level) can be used to estimate the detection limit for water abundance. The average SNR for the M^3 data is ~800 and ~300 at the equatorial and polar regions, respectively (52). Assuming that the albedo near 3 µm has a value near 0.2, and assuming that the sizes of the grains are 60 to 80 µm, this translates to an idealized detection limit of ~6 ppm at the equatorial regions and ~18 ppm at the polar regions. Therefore, we adopted an estimate of 20 ppm as our detection limit for the assumptions described here.

Effects of M^3 optical periods and detector temperature
The M^3 data were acquired in five optical periods (OP1A, OP1B, OP2A, OP2B, and OP2C) (52), during which instrument behavior and measurement conditions varied. Mosaics of images acquired during different optical periods may thus exhibit more variation across image boundaries than mosaics based on data acquired during a single optical period. The M^3 detector temperature also changed at different optical periods, which may have affected the performance of the detector (52), and M^3 images were thus classified into "cold" and "hot" groups (52). Mosaics of M^3 images acquired under the cold detector condition may be of higher quality than those acquired when the detector temperature was higher (hot) (52). Mosaics of M^3

images acquired in a single optical period (OP2C, best global coverage) and under hot and cold conditions were examined to verify that our observations and interpretations were not affected by these instrumental issues (fig. S6).

Mapping lunar surface water with M³ images acquired at different local time

The local hours of pixels of all M³ data were calculated from their respective solar azimuth angle (a), solar zenith angle (i), and the Sun declination angle ($d = 1.5°$) using the equation $h = sin^{-1}(sina * sini/cosd)$; h is the local hours in angles between $-\pi/2$ and $\pi/2$, while $-\pi/2$ and $\pi/2$ are set to 6:00 and 18:00, respectively. Only the M³ data acquired when the sensor temperature was appropriately low (cold) were used to assess the diurnal variation of lunar surface water. M³ pixels with acquisition time at 6:00 to 10:00, 10:00 to 14:00, and 14:00 to 18:00 were marked as morning, noon, and afternoon, respectively. The mosaics of morning, noon, and afternoon images and their respective acquisition times are presented in fig. S3. Part of the region of overlapping pixels (red box outlined in fig. S7) was not used to assess diurnal variations because the reflectance spectra from OP2A and OP2C in this region exhibit discrepancies at wavelengths of <2.6 µm (that is, outside of the water absorptions). Data in the remainder of the region of overlapping data did not exhibit these issues, despite being from different optical periods, and were used for the diurnal variation analysis.

SUPPLEMENTARY MATERIALS

Supplementary material for this article is available at http://advances.sciencemag.org/cgi/content/full/3/9/e1701471/DC1

Supplementary Text

fig. S1. The linear trends between ESPAT and weight % H₂O for materials typifying the lunar surface.

fig. S2. Crystalline plagioclase exposures identified in the M³ data by Donaldson Hanna et al. (36) overlain on map of lunar surface water derived from the M³ data.

fig. S3. The water content (ESPAT) mapped by M³ at three different lunar local time and the respective acquisition time of M³ data.

fig. S4. Filtering of the M³ data due to spectral artifacts affecting bands 47 and 74.

fig. S5. Filtering of the M³ data by SNRI (see Methods for details).

fig. S6. The global water map (ESPAT) of OP2C and maps acquired at different sensor temperatures.

fig. S7. Examples of spectral discrepancies (overall reflectance level and spectral slope) between the M³ OP2A and OP2C data sets.

fig. S8. SSA spectra of anorthosite after continuum removal over the 2.5-µm to 3.8-µm-wavelength region for data acquired from results during the stepwise heating experiments.

fig. S9. Continuum-removed reflectance spectra of MORB glass samples.

table S1. Results from select pyrolysis measurements that were performed on lunar regolith, mineral separates, agglutinates, and rocks sampled from the Apollo 11, 12, 14, 15, 16, and 17 landing sites.

table S2. SIMS measurements of water content (and δD values) for select Apollo samples that were used to generate Fig. 2.

Reference (58–64)

REFERENCES AND NOTES

1. J. R. Arnold, Ice in the lunar polar regions. *J. Geophys. Res.* **84**, 5659–5668 (1979).
2. H. Ducati, S. Kalbitzer, J. Kiko, T. Kirsten, H. W. Müller, Rare gas diffusion studies in individual lunar soil particles and in artificially implanted glasses. *Moon* **8**, 210–227 (1973).
3. S. Epstein, H. P. Taylor Jr., The concentration and isotopic composition of hydrogen, carbon and silicon in Apollo 11 lunar rocks and minerals. *Geochim. Cosmochim. Acta* **1**, 1085–1096 (1970).
4. K. Watson, B. C. Murray, H. Brown, The behavior of volatiles on the lunar surface. *J. Geophys. Res.* **66**, 3033–3045 (1961).
5. E. H. Hauri, A. E. Saal, M. J. Rutherford, J. A. Van Orman, Water in the Moon's interior: Truth and consequences. *Earth Planet Sci. Lett.* **409**, 252–264 (2015).

6. R. Tartèse, M. Anand, F. M. McCubbin, S. M. Elardo, C. K. Shearer, I. A. Franchi, Apatites in lunar KREEP basalts: The missing link to understanding the H isotope systematics of the Moon. *Geology* **42**, 363–366 (2014).
7. K. L. Robinson, G. J. Taylor, Heterogeneous distribution of water in the Moon. *Nat. Geosci.* **7**, 401–408 (2014).
8. A. E. Saal, E. H. Hauri, J. A. Van Orman, M. J. Rutherford, Hydrogen isotopes in lunar volcanic glasses and melt inclusions reveal a carbonaceous chondrite heritage. *Science* **340**, 1317–1320 (2013).
9. E. H. Hauri, T. Weinreich, A. E. Saal, M. C. Rutherford, J. A. Van Orman, High pre-eruptive water contents preserved in lunar melt inclusions. *Science* **333**, 213–215 (2011).
10. J. P. Greenwood, S. Itoh, N. Sakamoto, P. Warren, L. Taylor, H. Yurimoto, Hydrogen isotope ratios in lunar rocks indicate delivery of cometary water to the Moon. *Nat. Geosci.* **4**, 79–82 (2011).
11. F. M. McCubbin, A. Steele, E. H. Hauri, H. Nekvasil, S. Yamashita, R. J. Hemley, Nominally hydrous magmatism on the Moon. *Proc. Natl. Acad. Sci. U.S.A.* **107**, 11223–11228 (2010).
12. J. W. Boyce, Y. Liu, G. R. Rossman, Y. Guan, J. M. Eiler, E. M. Stolper, L. A. Taylor, Lunar apatite with terrestrial volatile abundances. *Nature* **466**, 466–469 (2010).
13. A. E. Saal, E. H. Hauri, M. L. Cascio, J. A. Van Orman, M. C. Rutherford, R. F. Cooper, Volatile content of lunar volcanic glasses and the presence of water in the Moon's interior. *Nature* **454**, 192–195 (2008).
14. E. Füri, E. Deloule, A. Gurenko, B. Marty, New evidence for chondritic lunar water from combined D/H and noble gas analyses of single Apollo 17 volcanic glasses. *Icarus* **229**, 109–120 (2014).
15. H. Hui, A. H. Peslier, Y. Zhang, C. R. Neal, Water in lunar anorthosites and evidence for a wet early Moon. *Nat. Geosci.* **6**, 177–180 (2013).
16. Y. Liu, Y. Guan, Y. Zhang, G. R. Rossman, J. M. Eiler, L. A. Taylor, Direct measurement of hydroxyl in the lunar regolith and the origin of lunar surface water. *Nat. Geosci.* **5**, 779–782 (2012).
17. T. B. McCord, L. A. Taylor, J.-P. Combe, G. Kramer, C. M. Pieters, J. M. Sunshine, R. N. Clark, Sources and physical processes responsible for OH/H₂O in the lunar soil as revealed by the Moon Mineralogy Mapper (M³). *J. Geophys. Res.* **116**, E00G05 (2011).
18. J. M. Sunshine, T. L. Farnham, L. M. Feaga, O. Groussin, F. Merlin, R. E. Milliken, M. F. A'Hearn, Temporal and spatial variability of lunar hydration as observed by the deep impact spacecraft. *Science* **326**, 565–568 (2009).
19. C. M. Pieters, J. N. Goswami, R. N. Clark, M. Annadurai, J. Boardman, B. Buratti, J.-P. Combe, M. D. Dyar, R. Green, J. W. Head, C. Hibbitts, M. Hicks, P. Isaacson, R. Klima, G. Kramer, S. Kumar, E. Livo, S. Lundeen, E. Malaret, T. McCord, J. Mustard, J. Nettles, N. Petro, C. Runyon, M. Staid, J. Sunshine, L. A. Taylor, S. Tompkins, P. Varanasi, Character and spatial distribution of OH/H₂O on the surface of the Moon seen by M³ on Chandrayaan-1. *Science* **326**, 568–572 (2009).
20. R. N. Clark, Detection of adsorbed water and hydroxyl on the Moon. *Science* **326**, 562–564 (2009).
21. A. Stephant, F. Robert, The negligible chondritic contribution in the lunar soils water. *Proc. Natl. Acad. Sci. U.S.A.* **111**, 15007–15012 (2014).
22. R. R. Hodges Jr., Ice in the lunar polar regions revisited. *J. Geophys. Res.* **107**, 6-1–6-7 (2002).
23. S. Li, R. E. Milliken, An empirical thermal correction model for Moon Mineralogy Mapper data constrained by laboratory spectra and Diviner temperatures. *J. Geophys. Res. Planets* **121**, 2081–2107 (2016).
24. J.-P. Combe, T. B. McCord, P. O. Hayne, D. A. Paige, paper presented at the EPSC-DPS Joint Meeting 2011, Nantes, France, 1 October 2011.
25. J. Bandfield, C. Edwards, M. Poston, R. Klima, Lunar H₂O/OH-distributions: Revised infrared spectra from improved thermal corrections, in *Proceedings of the 47th Lunar and Planetary Science Conference* (2016), vol. 47, p. 1594.
26. R. E. Milliken, J. F. Mustard, Estimating the water content of hydrated minerals using reflectance spectroscopy: I. Effects of darkening agents and low-albedo materials. *Icarus* **189**, 550–573 (2007).
27. R. N. Clark, C. M. Pieters, R. O. Green, J. W. Boardman, N. E. Petro, Thermal removal from near-infrared imaging spectroscopy data of the Moon. *J. Geophys. Res.* **116**, E00G16 (2011).
28. C. A. Hibbitts, G. A. Grieves, M. J. Dyar, A. B. Alexandrov, M. A. Johnson, T. M. Orlando, Thermal stability of water and hydroxyl on the surface of the Moon from temperature-programmed desorption measurements of lunar analog materials. *Icarus* **213**, 64–72 (2011).
29. A. S. Ichimura, A. P. Zent, R. C. Quinn, M. R. Sanchez, L. A. Taylor, Hydroxyl (OH) production on airless planetary bodies: Evidence from H⁺/D⁺ ion-beam experiments. *Earth Planet Sci. Lett.* **345**, 90–94 (2012).
30. B. Hapke, Bidirectional reflectance spectroscopy. I - Theory. *J. Geophys. Res.* **86**, 3039–3054 (1981).
31. D. S. McKay, G. H. Heiken, A. Basu, G. Blanford, S. Simon, R. Reedy, B. M. French, J. Papike, The Lunar regolith, in *Lunar Sourcebook: A User's Guide to the Moon*, G. H. Heiken, D. Vaniman, B. M. French, Eds. (Cambridge Univ. Press, 1991), pp. 285–356.

32. W. C. Feldman, S. Maurice, A. B. Binder, B. L. Barraclough, R. C. Elphic, D. J. Lawrence, Fluxes of fast and epithermal neutrons from lunar prospector: Evidence for water ice at the lunar poles. *Science* **281**, 1496–1500 (1998).

33. P. G. Lucey, D. T. Blewett, G. J. Taylor, B. R. Hawke, Imaging of lunar surface maturity. *J. Geophys. Res.* **105**, 20377–20386 (2000).

34. G. Heiken, D. Vaniman, B. M. French, *Lunar Sourcebook: A User's Guide to the Moon* (Cambridge Univ. Press, 1991).

35. L. T. Elkins-Tanton, T. L. Grove, Water (hydrogen) in the lunar mantle: Results from petrology and magma ocean modeling. *Earth Planet Sci.* **307**, 173–179 (2011).

36. K. L. Donaldson Hanna, L. C. Cheek, C. M. Pieters, J. F. Mustard, B. T. Greenhagen, I. R. Thomas, N. E. Bowles, Global assessment of pure crystalline plagioclase across the Moon and implications for the evolution of the primary crust. *J. Geophys. Res. Planets* **119**, 1516–1545 (2014).

37. L. R. Gaddis, M. I. Staid, J. A. Tyburczy, B. R. Hawke, N. E. Petro, Compositional analyses of lunar pyroclastic deposits. *Icarus* **161**, 262–280 (2003).

38. S. Li, thesis, Brown University, Providence, RI (2016).

39. R. E. Milliken, S. Li, Remote detection of widespread indigenous water in lunar pyroclastic deposits. *Nat. Geosci.* **10**, 561–565 (2017).

40. R. Klima, J. Cahill, J. Hagerty, D. Lawrence, Remote detection of magmatic water in Bullialdus Crater on the Moon. *Nat. Geosci.* **6**, 737–741 (2013).

41. N. Petro, P. J. Isaacson, C. M. Pieters, B. L. Jolliff, L. M. Carter, R. L. Klima, paper presented at the Lunar and Planetary Science Conference, The Woodlands, Texas, 2013.

42. S. Bhattacharya, S. Saran, A. Dagar, P. Chauhan, M. Chauhan, A. Ajai, S. K. Kumar, Endogenic water on the Moon associated with non-mare silicic volcanism: Implications for hydrated lunar interior. *Curr. Sci.* **105**, 685–691 (2013).

43. A. R. Hendrix, K. D. Retherford, G. R. Gladstone, D. M. Hurley, P. D. Feldman, A. F. Egan, D. E. Kaufmann, P. F. Miles, J. W. Parker, D. Horvath, P. M. Rojas, M. H. Versteeg, M. W. Davis, T. K. Greathouse, J. Mukherjee, A. J. Steffl, W. R. Pryor, S. A. Stern, The lunar far-UV albedo: Indicator of hydration and weathering. *J. Geophys. Res.* **117**, E12001 (2012).

44. T. A. Livengood, G. Chin, R. Z. Sagdeev, I. G. Mitrofanov, W. V. Boynton, L. G. Evans, M. L. Litvak, T. P. McClanahan, A. B. Sanin, R. D. Starr, J. J. Su, Moonshine: Diurnally varying hydration through natural distillation on the Moon, detected by the Lunar Exploration Neutron Detector (LEND). *Icarus* **255**, 100–115 (2015).

45. T. McClanahan, I. Mitrofanov, W. Boynton, G. Chin, L. Evans, R. Starr, A. Sanin, T. Livengood, R. Sagdeev, J. Bodnarik, Upper-latitude hydration of the moon's southern poleward-facing slopes, paper presented at Lunar and Planetary Science Conference, 2014.

46. G. R. Gladstone, K. D. Retherford, A. F. Egan, D. E. Kaufmann, P. F. Miles, J. W. Parker, D. Horvath, P. M. Rojas, M. H. Versteeg, M. W. Davis, T. K. Greathouse, D. C. Slater, J. Mukherjee, A. J. Steffl, P. D. Feldman, D. M. Hurley, W. R. Pryor, A. R. Hendrix, E. Mazarico, S. A. Stern, Far-ultraviolet reflectance properties of the Moon's permanently shadowed regions. *J. Geophys. Res.* **117**, E00H04 (2012).

47. R. E. Milliken, J. F. Mustard, Quantifying absolute water content of minerals using near-infrared reflectance spectroscopy. *J. Geophys. Res.* **110**, E12001 (2005).

48. G. Y. Kramer, S. Besse, D. Dhingra, J. Nettles, R. Klima, I. Garrick-Bethell, R. N. Clark, J.-P. Combe, J. W. Head III, L. A. Taylor, C. M. Pieters, J. Boardman, T. B. McCord, M³ spectral analysis of lunar swirls and the link between optical maturation and surface hydroxyl formation at magnetic anomalies. *J. Geophys. Res.* **116**, E00G18 (2011).

49. T. D. Glotch, J. J. Hagerty, P. G. Lucey, B. R. Hawke, T. A. Giguere, J. A. Arnold, J.-P. Williams, B. L. Jolliff, D. A. Paige, The Mairan domes: Silicic volcanic constructs on the Moon. *Geophys. Res. Lett.* **38**, L21204 (2011).

50. T. D. Glotch, P. G. Lucey, J. L. Bandfield, B. T. Greenhagen, I. R. Thomas, R. C. Elphic, N. Bowles, M. B. Wyatt, C. C. Allen, K. D. Hanna, D. A. Paige, Highly silicic compositions on the Moon. *Science* **329**, 1510–1513 (2010).

51. M. D. Dyar, C. A. Hibbitts, T. M. Orlando, Mechanisms for incorporation of hydrogen in and on terrestrial planetary surfaces. *Icarus* **208**, 425–437 (2010).

52. R. Green, C. Pieters, P. Mouroulis, M. Eastwood, J. Boardman, T. Glavich, P. Isaacson, M. Annadurai, S. Besse, D. Barr, B. Buratti, D. Cate, A. Chatterjee, R. Clark, L. Cheek, J. Combe, D. Dhingra, V. Essandoh, S. Geier, J. N. Goswami, R. Green, V. Haemmerle, J. Head, L. Hovland, S. Hyman, R. Klima, T. Koch, G. Kramer, A. S. K. Kumar, K. Lee, S. Lundeen, E. Malaret, T. McCord, S. McLaughlin, J. Mustard, J. Nettles, N. Petro, K. Plourde, C. Racho, J. Rodriquez, C. Runyon, G. Sellar, C. Smith, H. Sobel, M. Staid, J. Sunshine, L. Taylor, K. Thaisen, S. Tompkins, H. Tseng, G. Vane, P. Varanasi, M. White, D. Wilson, The Moon Mineralogy Mapper (M³) imaging spectrometer for lunar science: Instrument description, calibration, on-orbit measurements, science data calibration and on-orbit validation. *J. Geophys. Res.* **116**, E00G19 (2011).

53. M. J. Poston, G. A. Grieves, A. B. Aleksandrov, C. A. Hibbitts, M. D. Dyar, T. M. Orlando, Water interactions with micronized lunar surrogates JSC-1A and albite under ultra-high vacuum with application to lunar observations. *J. Geophys. Res. Planets* **118**, 105–115 (2013).

54. B. Hapke, *Theory of Reflectance and Emittance Spectroscopy* (Cambridge Univ. Press, 1993).

55. R. E. Milliken, J. F. Mustard, Estimating the water content of hydrated minerals using reflectance spectroscopy: II. Effects of particle size. *Icarus* **189**, 574–588 (2007).

56. R. E. Milliken, thesis, Brown University, Providence, RI (2006).

57. C. De Boor, *A Practical Guide to Splines* (Springer, 1978), vol. 27.

58. K. Shimizu, A. E. Saal, C. E. Myers, A. N. Nagle, E. H. Hauri, D. W. Forsyth, V. S. Kamenetsky, Y. Niu, Two-component mantle melting-mixing model for the generation of mid-ocean ridge basalts: Implications for the volatile content of the Pacific upper mantle. *Geochim. Cosmochim. Acta* **176**, 44–80 (2016).

59. L. Merlivat, M. Lelu, G. Nief, E. Roth, Deuterium, hydrogen, and water content of lunar material, in *Proceedings of the Fifth Lunar Conference* (1974), vol. 2, pp.1885–1895.

60. S. Epstein, H. P. Taylor Jr., The isotopic composition and concentration of water, hydrogen, and carbon in some Apollo 15 and 16 soils and in the Apollo 17 orange soil, in *Proceedings of the Fourth Lunar Science Conference* (1973), vol. 4, pp. 1559.

61. I. Friedman, J. R. O'Neil, J. D. Gleason, K. Hardcastle, The carbon and hydrogen content and isotopic composition of some Apollo 12 materials, in *Proceedings of the Second Lunar Conference* (1971), vol. 2, pp. 1407–1415.

62. I. Friedman, J. R. O'neil, L. H. Adami, J. D. Gleason, K. Hardcastle, Water, hydrogen, deuterium, carbon, carbon-13, and oxygen-18 content of selected lunar material. *Science* **167**, 538–540 (1970).

63. S. Epstein, H. Taylor Jr., O¹⁸/O¹⁶, Si³⁰/Si²⁸, C¹³/C¹², and D/H studies of Apollo 14 and 15 samples, in *Proceedings of the Third Lunar Science Conference* (MIT Press, 1972), vol. 2, pp. 1429–1454.

64. I. Friedman, K. G. Hardcastle, J. D. Gleason, Water and carbon in rusty lunar rock 66095. *Science* **185**, 346–349 (1974).

Citation: S. Li, R. E. Milliken, Water on the surface of the Moon as seen by the Moon Mineralogy Mapper: Distribution, abundance, and origins. *Sci. Adv.* **3**, e1701471 (2017).